FST10-128R1 Final

Forward Modeling of Motional Stark Effect Spectra

A. Dinklage, R. Reimer, R. Wolf, the Wendelstein 7-X Team*

Max-Planck-Institut für Plasmaphysik, EURATOM-Association

Wendelsteinstr. 1, Greifswald, Germany

M. Reich, the ASDEX Upgrade Team

Max-Planck-Institut für Plasmaphysik, EURATOM-Association

Boltzmannstr. 2, Garching, Germany

(Dated: September 28, 2010)

Abstract

A forward model for Motional Stark effect spectra is developed. The forward model includes beam attenuation and considers the detection of partially polarized light. The forward model is applied to simulate spectra for Wendelstein 7-X. A fit version is used to analyze data from experimental spectra from ASDEX Upgrade. The fit validates the model and enhances the confidence in the simulation. The structure and the content of the model is described to allow modular implementations to guide physics-based diagnostic designs.

PACS numbers: 52.55.Pi

*Electronic address: dinklage@ipp.mpg.de

I. INTRODUCTION

Quantitative simulations of experimental data expected for future fusion devices require synthetic diagnostics. The resulting virtual instruments can be effectively used to guide the design of diagnostics based on the underlying physics. For existing set-ups, virtual instruments can be used for the simulation of measurements and thus measuring capabilities can be assessed, e.g., by evaluating spurious effects. Moreover, diagnostic upgrades or routine maintenance of diagnostics can be assessed by performance checks using the virtual instruments. When using a suite of synthetic diagnostics for the same physical quantity, the approach may also contribute to data validation by providing the possibility of cross-checks.

Probabilistic models of measurements naturally lead to synthetic diagnostics [1]. A mathematical model to describe the error statistics of a measurement is the *likelihood* of the data. The likelihood function of the data is one key ingredient for Bayesian data analysis [2, 3]. A central element of the likelihood is the forward model which maps deterministically all quantities and measurement parameters on the data. This is what synthetic diagnostics are supposed to do.

The specific example discussed in this paper is part of a broader approach which investigates requirements for synthetic diagnostics for next step, steady-state fusion devices where increasing challenges are posed to diagnostics. Examples of diagnostic applications are machine protection, plasma control and physics evaluation which rely on diagnostic capabilities. Such steady-state devices demand much higher reliability and robustness due to the extended pulse lengths of the devices. In addition, high and sustained neutron fluxes may lead to new phenomena including radiation induced luminescence or radiation induced conductivity. Effects on measurement accuracy, resolution and lifetime needs to be assessed to comply with requirements for quantitative physics evaluation of experiments [4].

As seen by the ITER requirements for data analysis, which envisage an integrated design for diagnostics [5], simulations are to keep up with highest demands on the confidence in the diagnostics models. Fusion diagnostics design is assumed to be both as predictive and as reliable as possible. These kinds of requirements have been addressed in related analyses done for Wendelstein 7-X [6]. With the accomplishment of an integrated design concept, a suite of virtual instruments is expected to be viable. This suite can be regarded as a flight-simulator tool that allows diagnosticians to assess whether diagnostic units comply with the

required measuring capabilities. Since, in addition, the impact of foreseeable constraints, possible faults or unwanted effects can be simulated, this approach is preferable to trial-and-error steps.

This paper discusses the specific implementation of a general forward model for future spectral Motional Stark effect (MSE) measurements on Wendelstein 7-X. First spectrally resolved MSE measurements have been reported in [7]. Forward simulations of an active polarimetry Motional Stark effect diagnostics [8] have been reported by [9]. The simulation of a spectrally resolved Motional Stark effect diagnostic are specifically treated in [9–16]. MSE is planned to measure q-profiles to control the current profiles in ITER [4]. Simulations for ITER Motional Stark effect diagnostics are reported in [17]. Partly overlapping, partly newly developed, the forward model presented here involves a collisional-radiative beam-plasma model simulating the beam attenuation. Alignment effects [18, 19] and resulting deviations in emission line ratios are not considered in the forward model but the model is structured to include respective model extensions. In a fit version of the code, a parameter involving corresponding deviations (polarization factor) is included. For the simulations, the effect of alignment has been assessed by a correction to the simple collisional-radiative beam-plasma model. A full simulation of polarization properties employing the Müller-matrix formalism for partially polarized light is implemented. This sub-model can be transferred to other spectroscopic measurements. The code is structured and set-up to be integrated in Bayesian analyses. Thereby, device dependent parameters are separated from the model making the code device independent similar to the codes reported in [10, 11]. Moreover, simplifications of time-consuming submodules were implemented to allow diagnostic optimization studies [20] at feasible computational times.

In order to validate the chosen version of the forward model against experimental data, MSE spectra from ASDEX Upgrade are analyzed using a fit-version of the forward model. This approach is chosen to enhance the confidence in the forward model while its structural design tries to emphasize the possibility to transfer individual parts of the model to other applications.

II. MSE FORWARD MODEL

The forward function is a deterministic mathematical representation of a measurement (free from errors). Since the forward function enters the misfit distribution of the data, the forward function is also a key element for the probabilistic description of measurements. To simulate data for future devices, predictive simulations are used to simulate the measurements. Equilibrium calculations give the $\vec{B}$ field, plasma profiles are used to determine the beam excitation. The result of the simulation of the measurement are the data $\mathcal{D}$. Fig. 1 display a flow chart showing the elements entering the simulation of the spectral MSE measurements.

The flow chart gives also a rough guideline for the modularization of the forward model. Each element can be regarded as a sub-part of the model. For the implementations of the sub-models, the arrows indicate interfaces. The interface define the required content for the neighboring sub-part. Keeping a more refined sub-model compliant with the interface definitions allows one to exchange the sub-parts rather than setting up a complete new forward model. The model can be used for simulation, analysis and diagnostics design and optimization as discussed above.

A. From physics effects ...

The Motional Stark effect is the Stark splitting in the Lorentz field due to the electric field $\vec{F}$ in the frame of a fast beam moving in a strong magnetic field. $\vec{F}$ consists of a Lorentz field, the component of interest in MSE diagnostics, and the radial electric field. A convenient choice is the spectroscopy of the linear Stark effect on hydrogen isotopes for fusion diagnostics; the quadratic Stark effect leads to more complicated effects [21]. For Balmer-α spectroscopy with beam energies of the order of 50 keV/amu and magnetic fields of 2.5 T, the energy shift ΔE_n in the Stark multiplet of Hydrogen isotopes can be well described by the Epstein-Schwarzschild formula [22]:

$$\Delta E_n\,(\mathrm{eV}) = 7.94198 \times 10^{-7} \times |\vec{F}|\,(\mathrm{V\,m^{-1}})\, n\,(n_1 - n_2) \tag{1}$$

where n is the principal quantum number and n_1 and n_2 are parabolic quantum numbers. The influence of $\vec{B}$ in the moving frame has been considered by, e.g., [12, 18, 23]. For this

study, the combined Stark-Zeeman effect is not considered since it leads to only minor deviations from the linear Stark effect. The Stark multiplet consists of $\Delta m = 0$ (π) and $\Delta m = \pm 1$ ($\sigma^{\pm}$) transitions where m are the magnetic projection quantum numbers. The σ- and π-components are linearly or elliptically polarized depending on the direction of observation with respect to the electric field vector $\vec{F}$.

To start with the forward model, the signal level measured $\mathcal{D}$ by a pixel of a CCD chip is given by:

$$\mathcal{D}(\text{pixel}) = \varsigma\,(\text{pixel}) \times \mathbf{\Pi} \times \int_{A_p} \int_{\Omega} \frac{\Delta\mathcal{L}\,(\text{pixel}(\lambda))}{\Delta\text{pixel}}\,\cos\zeta\; dA_p\, d\Omega \tag{2}$$

The dispersion relation of the spectrometer pixel = pixel(λ) is determined by wavelength calibration measurements. The radiance $\mathcal{L}$ is the radiant flux per unit projected area observed at the boundary of the plasma dA_p and solid angle Ω. Later, the radiance is represented by a Stokes vector $\vec{\mathcal{L}}$ is used to represent to treat the polarization states of partially polarized plasma emission [24]. $\Delta\mathcal{L}$ refers to the wavelength interval covered by a pixel with width Δpixel. ζ is the angle enclosed by the line of sight and the normal vector of the surface A_p. Here the emission will be integrated along a line of sight through an optically thin plasma. The line integration will enter the radiance (see below) and the observed plasma surface A_p is given by the entendue $\mathcal{T} \approx A_s\Omega_m$ in the direction of the line-of-sight. Therefore, the angle ζ needs not accounted for ($\cos\zeta = 1$). Practically, $\mathcal{T}$ is limited by the observation optics [25]. A_s is the most limiting cross section in the observation optics and Ω_m is the corresponding solid angle. The operator $\mathbf{\Pi}$ accounts for polarization dependent transmission of the observation optics. The factor ς is the sensitivity which contains the quantum efficiency (photo electron per photon) and the amplification of the detector (counts per photo electron).

The radiance $\mathcal{L}$ represents the radiation *quasi* from an emitting surface. $\mathcal{L}$ is related to the line integral of the local emission coefficient ε along the line of sight L; writing the emission coefficient as a Stokes vector accounts for the polarization of the light:

$$\mathcal{L} = \int_L \varepsilon(s)\, ds \tag{3}$$

s is a coordinate along the line-of-sight. Radiation transport is neglected since the plasma is optically thin at wavelengths of the MSE spectra. Provided the variations of the observed cross sections A_p are small and the emission coefficient ε across the line of sight are small,

Eq.2 becomes:

$$\mathcal{D}(\text{pixel})\Delta\text{pixel} = \varsigma\,(\text{pixel}) \times \mathcal{T} \times \mathbf{\Pi} \times \int_L \Delta\varepsilon\,(s,\,\text{pixel}(\lambda))\;ds \tag{4}$$

So far, the forward model contains only algebraic operations representing a model for the detection of partially polarized light. To link the signal with the beam excitation process, physical models for the emission coefficient being represented as a Stokes vector $\vec{\varepsilon}$ need to be provided. A first, simplified model consists of the MSE spectrum, the charge exchange emission from the beam. This simple model disregards beam particle diffusion (beam halo) or effects resulting from fast ions. The motivation of this simplification results from the data analysis described later: it gives a reasonable description of the data and it avoids, e.g., modeling of fast ion charge exchange processes requiring large computational effort. The simple MSE model reads:

$$\vec{\varepsilon}(s,\,\lambda) \;=\; \vec{\varepsilon}_{MSE}(s,\,\lambda) + \vec{\varepsilon}_{CX}(s,\,\lambda) + \text{const} \tag{5}$$

where a constant background due to Bremsstrahlung is accounted for.

The simple forward model for the emission coefficient $\Delta\varepsilon\,(s,\,\text{pixel})$ can be readily extended to include further effects:

$$\begin{aligned}\vec{\varepsilon}(s,\lambda) \;=\; &\vec{\varepsilon}_{MSE}(s,\,\lambda) + \vec{\varepsilon}_{halo}(s,\,\lambda) + \vec{\varepsilon}_{FIDA}(s,\,\lambda) + \ldots \\ &\vec{\varepsilon}_{edge}(s,\,\lambda) + \vec{\varepsilon}_{Imp}(s,\,\lambda) + \vec{\varepsilon}_{BS}(s,\,\lambda)\end{aligned} \tag{6}$$

In this more complete model, the emission coefficient is assumed to consist of contributions from the Motional Stark effect (MSE), charge exchange of the plasma with the beam also covering fast ions ($FIDA$) (this contribution includes ε_{CX}), light from the beam halo ($halo$), emission from the cold plasma edge ($edge$), impurity lines (Imp) and Bremsstrahlung background (BS). All components contribute to different polarization states p.

The comparison of Eq. 5 with Eq. 6 reflects how the concept of modular subparts can be assigned to physical submodels. In the case considered here, submodels can be either exchanged (ε_{CX} by ε_{FIDA}) or included.

On the way to a specific implementation, we write down explicit dependencies of the individual components:

$$\vec{\varepsilon}_{MSE}(s,\,\lambda) \;=\; \sum_{\alpha}\left(\frac{hc}{4\pi\lambda}\,\vec{S}_{\pi}\,\sum_{\pi} n^{(n=3,\pi)}_{beam,\,\alpha}(s)\,A_{\pi}\,\mathcal{P}_b(s,\,\lambda,\,\lambda_{\pi,\alpha})\,\ldots\right.$$
$$\left.+\frac{hc}{4\pi\lambda}\,\vec{S}_{\sigma^{\pm}}\,\sum_{\sigma^{\pm}} n^{(n=3,\sigma^{\pm})}_{beam,\,\alpha}(s) A_{\sigma}\,\mathcal{P}_b(s,\,\lambda,\,\lambda_{\sigma^{\pm},\alpha})\right) \tag{7}$$

$$\vec{\varepsilon}_{CX}(s,\,\lambda) \;=\; n^{(n=3)}_{plasma}(s)\frac{hc}{4\pi\lambda}\,\vec{S}_{CX}\,A_{n=3}\mathcal{P}_p(\lambda) \tag{8}$$

$$\vec{\varepsilon}n_{halo}(s,\,\lambda) \;=\; n^{(n=3)}_{halo}(s)\frac{hc}{4\pi\lambda}\,\vec{S}_{halo}\,A_{n=3}\mathcal{P}_h(\lambda) \tag{9}$$

$$\vec{\varepsilon}n_{edge}(s,\,\lambda) \;=\; n^{(n=3)}_{edge}(s)\frac{hc}{4\pi\lambda}\,\vec{S}_{edge}\,A_{n=3}\mathcal{P}_e(\lambda) \tag{10}$$

$$\vec{\varepsilon}_{FIDA}(s,\,\lambda) \;=\; n^{(n=3)}_{FIDA}(s)\frac{hc}{4\pi\lambda}\,\vec{S}_{FIDA}\,A_{n=3}\mathcal{P}_{FIDA}(\lambda) \tag{11}$$

$$\vec{\varepsilon}n_{Imp}(s,\,\lambda) \;=\; \sum_{Imp} n_{Imp}(s)\frac{hc}{4\pi\lambda}\,\vec{S}_{Imp}\,A_{imp}\mathcal{P}_i(\lambda,\,\lambda_{Imp}) \tag{12}$$

$$\vec{\varepsilon}_{BS}(s,\,\lambda) \;=\; 4.51\times10^{-39}\,Z^2\left(\frac{k_B T_e}{E_{Ryd}}\right)^{1/2} n_Z n_e\,\vec{S}_{BS} \tag{13}$$

α indicates the beam energy components. $\vec{S}$ are the Stokes vectors for the different light emission processes. Except for MSE, the light is assumed to be unpolarized. The $\mathcal{P}$ are normalized profile functions reflecting the shapes of spectral lines as observable from the plasma. $\mathcal{P}$ is a function of the coordinate s along the line of sight, λ and - in case of discrete lines - of the line centers. Z is the effective charge of the plasma, E_{Ryd} is the Rydberg energy of hydrogen. The Einstein coefficients A refer to upper levels as indicated.

At this point, a discussion of the components of the emission coefficients is helpful. The MSE component is the most prominent part of a performance study. The charge exchange (CX or $FIDA$) neutrals result in broad line contributions potentially overlapping with the MSE multiplet. Therefore, its is crucial to consider the CX part of the spectrum. Neutral particles moving into the observation volume forming a beam halo certainly affect the spectrum but are considered to be in the order of magnitude of charge exchange contributions or even less. The detailed description of the halo contribution is subject to later model extensions. Here, it will be modeled by an additional broad CX component. The emission of cold edge neutrals is large, but can be suppressed in the spectrometer [26]. To predict diagnostic performance, complicated mechanisms like the fast-ion D_α emission require comparable high modeling effort but are known from experiments to result in a small contribution. Therefore they will be left out in this study. Impurity lines are assumed to be separated and do

not affect the spectrum in the MSE region. The Bremsstrahlung background (ε_{BS})is small in amplitude, but the small broadband contribution summing up over the entire spectrum affects the global uncertainty of the forward model considerably.

Now, the remaining part for the simulation of MSE spectra in future devices is the signal amplitude. According to Eqs. 7 - 11, the signal amplitude requires the calculation of the densities of light emitting particles. This can be done by a collisional-radiative beam plasma model (CRM) as depicted in Fig. 2 showing the levels and their respective population and depopulation paths. Main excitation processes are heavy particle collisions along with electron collisions. Moreover, the proton collisions also lead to the population of neutrals by charge exchange and excitation transfer. Beam attenuation is due to beam ionization and, again, charge exchange. Radiative processes lead to the decay of excited particles and are used to quantify the spectroscopic signal. The resulting CRM contains all densities ($\vec{n}$) of considered states both in the beam and the plasma:

$$\frac{d}{dx}\vec{n} = \frac{1}{v_B}\mathbf{A}\vec{n} \tag{14}$$

where v_B is the beam velocity and $\mathbf{A}$ contains the rate coefficients for the collisional and radiative processes as indicated in Fig. 2 to be solved for the beam components α at full, half and third energy. The transition rates depend on the plasma parameters.

Solving the CRM is necessary to predict signal heights and their dynamics along the beam. For this simulation, the stationary solution ($\partial/\partial t = 0$) of Eq.14 is employed. For data analysis, it is feasible to describe the signal amplitude by a fit-parameter. Once additional data on densities and temperatures and information on the plasma equilibrium became available a more comprehensive fit became possible as demonstrated in the concept of Integrated Data Analysis [6].

B. ... to forward calculation

Now a signal can be calculated from equilibrium information $\vec{B}(\vec{x})$ and profiles of $n_e(r)$, $n_i(r)$, $T_e(r)$, $T_i(r)$, $Z(r)$ and $E_r(r) = \langle\nabla_r\phi(r)\rangle$. The equilibrium yields the mapping from flux surfaces to real space coordinates $\vec{x} = \vec{x}(r)$ and metric coefficients $|g|$ to calculate real space radial electric fields $\vec{E}_r(\vec{x}) = \langle\partial/\partial r\phi(r)\rangle\,\vec{e}_r$.

To determine beam related effects, the beam velocity $\vec{v}_b$, its divergence angle γ_b and the

density composition in full beam energy E, half $E/2$ and third $E/3$ energy is taken as an experimental parameter as well as the port-through power P_b.

The collisional radiative model (CRM, Eq. 14) is solved as an initial value problem with all beam particles being in the ground state before the beam enters the plasma. The rate coefficients as functions of densities and temperatures were taken from fit expressions [27]. The solution gives the densities $n_{beam}^{(n=3,\pi)}(s)$, $n_{beam}^{(n=3,\sigma^{\pm})}(s)$ for Eq. 7 and $n_{plasma}^{(n=3)}(s)$ for Eq. 8 assuming a statistical multiplet distribution. More sophisticated collisional radiative models, e.g. to account for alignment effects [18, 19], could be used instead.

To complete the necessary information for Eq. 7, the Einstein coefficients for the sublevels A_π and $A_{\sigma^\pm}$ are taken from solutions of the Schrödinger equation [28]. The profile $\mathcal{P}_b$ is the Doppler width of the multiplet lines resulting from the beam divergence from a Gaussian intensity profile of the injected beam. This broadening has been found in experiments to be the leading broadening effect, but more detailed assumptions can be added straight-forward. The line shifts of the multiplet components λ_π and $\lambda_{\sigma^\pm}$ result from the line splitting due to the electric field

$$\vec{F}(s(\vec{x})) = \vec{v}_b \times \vec{B}(\vec{x}) + \vec{E}_r(\vec{x}) \tag{15}$$

and a Doppler shift due to the beam motion. The line splitting is calculated from the Schwarzschild-Epstein formula. The Doppler shift is determined from the line-of-sight and the beam geometries.

For the charge exchange component, the line emission profile $\mathcal{P}_p$ is determined from the ion temperature; Doppler shift due to rotation are not taken into account for Wendelstein 7-X simulations, but are allowed to occur for the tokamak data. The Einstein-coefficient $A_{n=3}$ is summed from the multiplet resolved Einstein coefficients.

The polarization state is determined from the sums in Eq. 7, i.e. the π components are linearly polarized with respect to the quantization axis given by $\vec{F}$. Accordingly, the $\sigma^\pm$ components are circularly polarized in the direction of $\vec{F}$. The charge exchange emission and the Bremsstrahlung is assumed to be unpolarized.

At this point, the polarization-state resolved and wavelength dependent local emission coefficient $\vec{\varepsilon}(s,\, \lambda)$ can be determined. The line-of-sight integration $\int_L \Delta\vec{\varepsilon}(s,\, \mathrm{pixel}(\lambda))\; ds$ is considered by the length of the optical path transversing the beam. With given etendue $\mathcal{T}$ and pixel sensitivity ς, the polarization dependent transmission $\mathbf{\Pi}$ are left to determine the

data $\mathcal{D}$ in Eq. 4.

Since the forward model will result in partially polarized light, $\mathbf{\Pi}$ is formulated as a chain of Müller matrices applied to the Stokes vector $\vec{S}$. The definition follows Ref. [24]:

$$\vec{S} = \begin{bmatrix} I \\ Q \\ U \\ V \end{bmatrix} = \begin{bmatrix} \langle E_\parallel E_\parallel^* + E_\perp E_\perp^* \rangle \\ \langle E_\parallel E_\parallel^* - E_\perp E_\perp^* \rangle \\ \langle E_\parallel E_\perp^* + E_\perp E_\parallel^* \rangle \\ i\langle E_\parallel E_\perp^* - E_\perp E_\parallel^* \rangle \end{bmatrix}. \tag{16}$$

where I represents the total radiance. Q, U and V are quantities describing the linearly and circularly polarized contributions of the total radiance. The electric field $\vec{E}$ of the observed light is given by:

$$\vec{E} = \vec{E}_0 \exp\left(i(kz - \omega t)\right) \tag{17}$$

$$\vec{E}_0 = E_\parallel \vec{e}_\parallel + E_\perp \vec{e}_\perp \tag{18}$$

where $\parallel$ and $\perp$ are orthogonal axes, both of which have components perpendicular to the light propagation.

In a frame given by a quantization axis ($\vec{e}_z$) parallel to the electric field $\vec{F}$, the electric field of light from $\Delta m = 0$ (π-) and $\Delta m = \pm 1$ (σ-) lines are:

$$\begin{aligned} \vec{E}_\pi &= E_z \vec{e}_z = 2^{-1/2}\, E_0 \exp\left(-i\omega t\right) \vec{e}_z \\ \vec{E}_\sigma &= E_x \vec{e}_x + E_y \vec{e}_y = 1/2\, E_0 \left(\exp\left(-i\omega t\right) \vec{e}_x \mp i \exp\left(-i\omega t\right) \vec{e}_y\right) \end{aligned} \tag{19}$$

The resulting Stokes vectors are:

$$\vec{S}_\pi = \frac{1}{2} I_0 \begin{pmatrix} \cos^2\theta \\ \cos^2\theta \\ 0 \\ 0 \end{pmatrix} \tag{20}$$

θ is the angle between the line of sight and $\vec{F}$. $\vec{S}_\pi$ reflects the emission anisotropy of the emission from a Hertzian dipole. For the $\sigma^\pm$-components one arrives at:

$$\vec{S}_{\sigma^{\pm}} = \frac{1}{4} I_0 \begin{pmatrix} 1 + \sin^2\theta \\ -1 + \sin^2\theta \\ 0 \\ \pm 2\sin\theta \end{pmatrix} \tag{21}$$

It is interesting to note that the Stokes vector $\vec{S}_{\Sigma}$ given by

$$\vec{S}_{\Sigma} = \vec{S}_{\pi} + \vec{S}_{\sigma^+} + \vec{S}_{\sigma^-} = \frac{1}{2} I_0 \begin{pmatrix} 1 + \sin^2\theta + \cos^2\theta \\ -1 + \sin^2\theta + \cos^2\theta \\ 0 \\ \sin\theta - \sin\theta \end{pmatrix} = I_0 \begin{pmatrix} 1 \\ 0 \\ 0 \\ 0 \end{pmatrix} \tag{22}$$

reflects Heisenberg's principle of optical stability: if the radiance of degenerate $\pi-$ and $\sigma-$ lines are emitted such that

$$\sum_{\pi} n_{\pi} A_{\pi} = \sum_{\sigma^+} n_{\sigma^+} A_{\sigma^+} = \sum_{\sigma^+} n_{\sigma^-} A_{\sigma^-} \tag{23}$$

then the emission is isotropic, i.e. $\vec{S}_{\Sigma}$ is independent from the observation direction expressed by θ. Although all elementary emission processes result in polarized light, the total emission is unpolarized for Q, U, $V = 0$ in Eq. 22. Wavelength separation due to external fields, however, changes the situation fundamentally. It is also interesting to note that the formulation of the Stokes vector contains any effect of emission anisotropy, which is sometimes also reflected by the sub-level resolved Einstein coefficients in text books [29]. However, deviations from statistical distributions are observed the larger the more the density decreases from about $n < 10^{20}\mathrm{m}^{-3}$ (e.g. [10, 19, 30]). In other words, even the wavelength integrated MSE emission is polarized.

In order to cover all observation geometries possible, the vibration ellipse is allowed to rotate with the line-of-sight as rotation axis (with angle ϕ). According to [24], the rotation can be expressed by a Müller matrix:

$$\mathcal{M}_{\phi} = \begin{bmatrix} 1 & 0 & 0 & 0 \\ 0 & \cos 2\phi & \sin 2\phi & 0 \\ 0 & -\sin 2\phi & \cos 2\phi & 0 \\ 0 & 0 & 0 & 1 \end{bmatrix} \tag{24}$$

Any additional optical element in the observation optics can be expressed by a Müller matrix and wavelength dependent transmission functions $\tau(\lambda)$. Müller matrices for ideal polarizers and retarders, respectively, can be found in [31]. Photo-elastic modulators, as a combination of rotating retarders and polarizers, can be expressed by the respective combination of time dependent Müller matrices. Optical fibers can be regarded as ideal depolarizers:

$$\mathcal{M}_{\text{fiber}} = \begin{bmatrix} 1 & 0 & 0 & 0 \\ 0 & 0 & 0 & 0 \\ 0 & 0 & 0 & 0 \\ 0 & 0 & 0 & 0 \end{bmatrix} \tag{25}$$

The operator representing the observation can be expressed as:

$$\mathbf{\Pi} = \tau(\lambda) \times \Pi_i \mathcal{M}_i \tag{26}$$

At this point, all model parameters have been specified and can be regarded to result either from physics modeling (predictive transport model, equilibrium), atomic data bases or atomic physics calculations or experimental settings. A summary of all parameters and quantities entering the forward model are given in Tabs. I and II.

III. FORWARD SIMULATION OF MSE SPECTRA FOR WENDELSTEIN 7-X

Now the forward model will be applied to cases for Wendelstein 7-X. First the density of light emitting particles is calculated. The required input quantities (cf. Tab. II) are taken from predictive transport simulations [32] and settings. Geometrical data were taken from CAD data. A CAD view of a possible MSE arrangement is shown in Fig. 3. Tab. I summarizes derived quantities in the model and the measurand, Tab. II contains the input parameters of the model.

With this input, the simplified collisional radiative beam-plasma model has been solved. The CRM used here was truncated to $n = 3$ to estimate the population densities in the light emitting states (MSE) and to simulate the beam attenuation (CX). For analyses, this model underestimates the $n = 3$ population and cannot resolve non-statistical distributions in sublevels. More detailed CRMs for beam particle populations are reported, e.g., in [19, 33]. For design purposes, however, the model yields reasonable rates of light emission and the

required dynamic detector resolution if the attenuated beam is observed along the beam-line. A beam-stopping model for deuterium beams has been reported in [34]. The simple model used here, however, is computationally fast allowing one to apply feasible optimization algorithms. Some results for the state resolved CRM (ten plasma and beam states in total) are shown in Fig. 4. For the simulation of a 60 keV hydrogen beam, more than 90% of the beam is deposited in the plasma. The main attenuation process are charge-exchange collisions and ionizing collisions with heavy particles. Yielding the measurand, the $n = 3$ densities are shown indicating a sharp rise in the emission intensity when the beam enters the plasma, decreasing to about one order of magnitude in the course of the beam. The more spurious light emission from $n = 3$ plasma atoms (due to charge exchange processes= increases slightly retarded but the total number of emission processes remain larger than the beam emission along most of the beam line.

For a cross check of the figures shown in Fig. 4, the maximum fraction of $n = 3$ beam particles (at $T = 2.8\,\mathrm{keV}$ and $n \approx 8\times10^{19}\,\mathrm{m}^{-3}$) was found to be $n_3/n_1 = 0.29\%$. Comparable calculations for stationary situations [35] give fractions of $n_3/n_1 \approx 0.28\%$ for $T = 2.8\,\mathrm{keV}$ and $n \approx 10 \times 10^{19}\,\mathrm{m}^{-3}$. In the plasma region, the simple model gives about 15% larger values than Ref. [35] indicating the error due to neglecting levels $n > 3$. For the design of diagnostics, the results indicate quantitatively the required dynamic range for light detection.

Motional Stark effect spectra for the geometry of the diagnostic beam planned for W7-X are shown in Figs. 5 and 6. The plots contain spectra for 16 spatial channels corresponding to the beam penetrating from lower beam coordinates; the beam emission of the outermost two channels is not excited due to vanishing plasma densities for the respective positions. For a representative discussion, we consider a channel corresponding to the gradient region of the plasma (bold red line in Figs. 5 and 6). Finite beam effects enter the simulations through the beam-divergence only. Further refinement of the simulation with regard to finite beam and finite observation cones are expected to broaden the multiplet emission further.A more detailed neutral beam model is required, e.g., for ITER, where the resulting emission profile of the individual multiplet components should even be expected to get structured rather than being a single-mode (Gaussian) profile [36].

The first left and center plot of Fig. 5 show the effect of the emission anisotropy and the observation geometry. The spectra consist of dominant peaks (for the discussed channel on the blue side) and a broad CX contribution. The dominant peaks correspond to the

central σ lines of the full, half and third energy component of the beam. Being broadened due to the beam divergence, the σ- and π-components cannot be resolved as separated lines. While the total number of emission processes is shown in the left plot, the MSE lines significantly decrease in the center plot reflecting the different emission characteristics of the differently polarized components. The unpolarized CX contribution, however, is unaffected (except for the etendue). The apparent ratio of dominant peaks, moreover, is changing. This indicates the contribution of π-lines from the full energy to overlap with the σ-lines of the half-energy spectrum. Thus, the overlapping components of different polarization from different beam energies may lead to misinterpretation if the radiance at the maximum of the lines is considered only.

The center and right plot of Fig. 5 show the effect of a reduced (half) beam divergence. Now, the π-components become visible, but again the apparent relative ratios of the dominant peaks change indicating again the necessity to account for all multiplet components properly.

To study the effect of polarizing elements, Fig. 6 shows the spectra after transversing different polarizers. Similar to the previously discussed cases, the effect of polarizing elements affects the line ratios. It is concluded from these results that MSE diagnostics require a quantitative consideration of both the polarization of emission as well as the polarizing properties of the observation optics.

Finally, Fig. 7 is to discuss and to estimate the effect of non-statistical distributions. Density dependent corrections for the upper state distributions have been taken from results of an elaborate CRM [19] (at $T = 3$ keV, $E = 50$ keV, $\vec{F} \perp v_{beam}$). The parameters aside the density differ somewhat from the parameters ion our simulations ($T_i \approx 4$ keV, $E = 60$ keV)), but the difference in the line ratios is considered to be representative. It can be seen, that the radiance maximum of the central σ-component is about 10% smaller while the π-components become up to 15 % larger due to non-statistical multiplets. The effect must be expected to increase if the densities become smaller than here ($n < 8 \times 10^{19}\, m^{-3}$). As a conclusion, the effect of non-statistical distributions is a correction in the order of 10% for the simulation of signals. For analyses, as shown in the next section, the ratio of π and σ components is a sensitive fit parameter. Consequently, a correct interpretation of this fit parameter needs to consider non-statistical distributions properly.

IV. VALIDATION OF THE FORWARD MODEL ON ASDEX-UPGRADE

To check the validity of the forward model, Eq. 5 has been fitted to experimental spectra. The set-up of the measurement is described in [26]. Purpose of the fit is to reproduce the shape of the spectra and to determine the value of the electric (Lorentz) field. Therefore and since an absolute calibration of the observation is underway, the CRM has not been solved for the fit but the beam intensity is taken into account by a fit factor.

Fig. 8 shows results for MSE spectra from ASDEX Upgrade. Gross features of a typical MSE spectrum can be clearly identified. The apparent difference to the number of peaks compared to the W7-X simulation (cf. e.g. Fig. 6) is due to different viewing geometries and beam energies making some π-components to appear as additional distinct lines. The MSE lines lie in the spectral region of about 653nm ... 655.5 nm. To suppress the high radiance D_α radiation from the plasma edge, a wire has been placed in the focal plane of the spectrometer as indicated by the shaded areas in Fig. 8. Nevertheless, charge exchange processes contribute to the spectrum with a broad emission reflecting the ion temperature. The fit gives central ion temperature of about 1.2 keV for the observation channels in the plasma center. To attain a good fit to the data, a second contribution at lower temperature needs to be included. Both contributions are allowed to be Doppler shifted reflecting plasma rotation. A more detailed assessment of the broad background lines is beyond the scope of this paper. As a third part of the spectrum, background Bremsstrahlung is subtracted as a constant off-set. Carbon impurity lines have been fitted; these lines seem to indicate plasma rotation as well.

Summarizing, the fit consists of three main parameters: the electric field, a polarization factor and the beam composition. The polarization factor is sought to reflect the direction of the electric field. It has been introduced to vary the relative intensities of π- and σ-components entirely for each polarization state. This single factor was found to be sufficient for the fit. The value of the resulting factor, however, cannot be explained by emission anisotropy only. Deviations might have their origin in atomic physics effects and/or the effect of polarizers in the observation optics (polarization dependent transmission). In order to disentangle the different effects, calibration measurements are underway.

The resulting electric field from the spectra can be compared to the Lorentz field from equilibrium calculations (CLISTE [37]). The MSE electric field is about 10% systematically

larger than the results from unconstrained equilibrium calculations. Such discrepancy has been reported in [38] and is presently under assessment. As the residuum (Fig. 8, lower panel) indicates, the present forward model shows systematic deviations in the blue side wing of the MSE component. This may indicate the influence of fast ion D_α emission [39]. Furthermore, the residuum shows oscillatory deviations in the region of the Stark multiplet. This is sought to result from non-Gaussian beam profiles of the neutral beam. From fits, a mean total effective divergence of $1.57° \pm 0.12°$ (1/e) has been derived. From the specified minimum divergence of the ASDEX Upgrade NBI (1.05°) [40], the beam focusing geometry ($0.40° \pm 0.06°$) and a rough estimate of the acceptance angle of the observation optics observed ($0.70° \pm 0.26°$) one arrives at an harmonic sum of $1.34° \pm 0.16°$ with an error also considering the apparatus width of the detection system. The values agree within a 1-σ error estimate. A more detailed neutral beam modeling with regard to the profile shape is under investigation. A NeI line at about 650.5 nm from wavelength calibration can be found in all spectra (not fitted).

Concluding, the fit of the forward model gave very reasonable agreement with the data (normalized $\chi^2/N \approx 10$; the error of the data has been determined by calibration measurements at varying radiance) indicating the leading order effects to be compliant with the choice of contributions in the Wendelstein 7-X forward model. Deviations have been figured out and are addressed for diagnostic improvements.

V. SUMMARY

A forward model for MSE spectra has been implemented. Simulations for spectra for Wendelstein 7-X have been performed. The required dynamic range of a detector can be derived from results of the collisional radiative beam-plasma model. The influence of observation geometry and polarizing effects in the detection optics shows the necessity to include the polarization properties both of emission and detection for Wendelstein 7-X example. Diagnostic amendments, e.g. improvements of beam divergence exemplify possible studies for diagnostic designs. Meeting with the requirement to enhance the confidence in the design, the validity of the model has been assessed by fitting the forward model to experimental data from ASDEX Upgrade. The model resulted in reasonable fits; this confirms the choice of leading order effects in the simulation.

The physics structure of the forward model implies a modular structure of the synthetic diagnostic software. Main parts of model modules are the beam-plasma interaction, physics of local light emission and spectroscopic detection. The model structure defines interface requirements for the sub-parts of the model. The implementation of the MSE forward model as a prototype of validated synthetic diagnostics employing unified software interfaces and re-usable software modules is underway.

Acknowledgements

This work has been has been conducted within the EFDA task WP10-DIA-05-01-03/IPP. The authors appreciate helpful discussions with J. Baldzuhn, R. Coelho, R. Fischer, J. Hobirk, A. Stäbler and U. von Toussaint. The authors would like to thank the referees for their comments and one reviewer for providing the authors with the unpublished document ITER-CXRS-CORE-UKAEA-Memo-0006.

---

[1] R. Fischer, A. Dinklage, and E. Pasch, Plasma Phys. Control. Fusion **45**, 1095 (2003).

[2] A. Gelman, J. Carlin, H. Stern, and D. Rubin, Baysian Data Analysis (Chapman Hall CRC, 1995).

[3] P. Gregory, Bayesian Logical Data Analysis for the Physical Sciences (Cambridge, 2005).

[4] A. Donné and et al., Nucl. Fusion **47**, S285 (2007).

[5] T. Caspar and et al., Fusion Sci. Technol. **X**, X (2010).

[6] A. Dinklage, R. Fischer, and J. Svensson, Fusion Sci. Technol. **46**, 355 (2004).

[7] R. Wolf, J. O'Rourke, A. Edwards, and M. Hellermann, Nucl. Fusion **33**, 663 (1993).

[8] F. Levinton, Rev. Sci. Instrum. **63**, 5157 (1992).

[9] M. F. M. De Bock, N. J. Conway, M. J. Walsh, P. G. Carolan, and N. C. Hawkes, Rev. Sci. Instrum. **79**, 10F524 (2008), ISSN 0034-6748.

[10] B. A., von Hellermann M., M. W., S. H.P., W. H., and Z. A., J. Phys. B **22**, L145 (1989).

[11] N. Hawkes and et al, Rev. Sci. Instrum. **70**, 894 (1999), ISSN 0034-6748.

[12] W. Mandl, R. C. Wolf, M. G. von Hellermann, and H. P. Summers, Plasma Phys. Control. Fusion **35**, 1373 (1993).

[13] R. Jaspers, B. Elzendoorn, A. Donné, and T. Soetens, Rev. Sci. Instrum. **72**, 1018 (2001).

[14] K. Jakubowska, M. De Bock, R. Jaspers, M. von Hellermann, and S. L., Rev. Sci. Instrum. **75**, 3475 (2004).

[15] K. Ida, M. Yoshinuma, K. Watanabe, T. Kobuchi, and K. Nagaoka, Rev. Sci. Instrum. **76** (2005), ISSN 0034-6748.

[16] H. Yuh, F. Levinton, S. Scott, and J. Ko, Rev. Sci. Instrum. **79**, 10F523 (2008).

[17] E. L. Foley, F. M. Levinton, H. Y. Yuh, and L. E. Zakharov, Rev. Sci. Instrum. **79**, 10F521 (2008), ISSN 0034-6748.

[18] A. Iwamae, A. Sakaue, M. Atake, K. Sawada, M. Goto, and S. Morita, Plasma Phys. Control. Fusion **51**, 115004 (2009).

[19] O. Marchuk, Y. Ralchenko, R. Janev, W. Biel, D. E., and U. A.M., J. Phys. B **43**, 011002 (2010).

[20] H. Dreier, A. Dinklage, R. Fischer, M. Hirsch, and P. Kornejew, Rev. Sci. Instrum. **79** (2008), ISSN 0034-6748.

[21] B. A. Pohlmeyer, A. Dinklage, and H.-J. Kunze, J. Phys. B **29**, 221 (1996).

[22] P. Heckmann and E. Träbert, Introduction to the Spectroscopy of Atoms (North-Holland, 1989).

[23] E. K. Souw and J. Uhlenbusch, Physica **122C**, 353 (1983).

[24] C. Bohren and D. Huffmann, Absorption and Scattering of Light by Small Particles (Wiley-VCH, 2004).

[25] H.-J. Kunze, Introduction to Plasma Spectroscopy (Springer, 2009).

[26] R. Reimer, A. Dinklage, J. Geiger, J. Hobirk, M. Reich, and R. Wolf, Contrib. Plasma Phys. **50** (2010).

[27] R. Janev and et al., Elementary Processes in Hydrogen-Helium Plasmas (Springer, 1987).

[28] W. Mandl, Ph.D. thesis, Technische Universitt Mnchen (1991).

[29] I. Sobelman, Atomic Spectra and Radiative Transitions (Springer, 1979).

[30] M. F. Gu, C. T. Holcomb, R. J. Jayakuma, and S. L. Allen, Rev. Sci. Instrum. **41** (2008), ISSN 0953-4075.

[31] W. Shurcliff, Polarized Light (Harvard University Press, 1962).

[32] Y. Turkin, H. Maassberg, C. Beidler, J. Geiger, and N. Marushchenko, Fusion Sci. Technol. **50**, 387 (2006).

[33] E. Foley and F. M. Levinton, Journal of Physics B-Atomic Molecular and Optical Physics **39**, 443 (2006), ISSN 0953-4075.

[34] H. Anderson, M. von Hellermann, R. Hoekstra, L. Horton, A. Howman, R. König, R. Martin, R. Olson, and H. Summers, Plasma Phys. Control. Fusion **42**, 781 (2000).

[35] I. Hutchinson, Plasma Phys. Control. Fusion **44**, 71 (2000).

[36] N. Hawkes, M. DeBock, N. Conway, and M. von Hellermann, 'Line Widths of the BES Spectra for the ITER CXRS Diagnostics', ITER-CXRS-CORE-UKAEA-Memo-0006 (2009) unpublished document.

[37] W. Schneider, P. Mc Carthy, K. Lackner, O. Gruber, K. Behler, P. Martin, and M. R., Fusion Eng. Design **48**, 127 (2000).

[38] N. A. Pablant, K. H. Burrell, R. J. Groebner, D. H. Kaplan, and C. T. Holcomb, Rev. Sci. Instrum. **79**, 10F517 (2008), ISSN 0034-6748.

[39] W. Heidbrink, K. Burrell, Y. Luo, N. Pablant, and R. E., Plasma Phys. Control. Fusion **46**, 1855 (2004).

[40] P. Franzen, W. Kraus, O. Vollmer, B. Heinemann, R. Riedl, E. Speth, and A. Stäbler, 26^{th} EPS Conf. on Contr. Fusion and Plasma Physics, ECA **23J**, 1557 (1999).

$\mathcal{D}$	data	
pixel	argument of data	
λ	wavelength	from calibration
$\vec{F}$	electric field	measurand
θ	angle of $\vec{F}$ with line of sight	derived quantity
$\vec{n}$	CRM state vector	derived quantity
n_{source}^{state}	population density of state by emission source	derived quantity
$\vec{S}$	Stokes vector	derived quantity
I, Q, U, V	Stokes vector components	
$\mathcal{L}$	radiance	derived quantity
ε	emission coefficient	derived quantity

TABLE I: Data, measurands and derived quantities in the MSE forward model.

$n_{e,\,i}(r)$	electron/ion density	transport model
$T_{e,\,i}(r)$	electron/ion temperature	transport model
$Z(r)$	effective ion charge	transport model
n_Z	impurity density	transport model
Φ	electrostatic potential	transport model
E_r	radial electric field	transport model
$\vec{B}$	magnetic field vector	equilibrium
$\|g\|$	metric coefficient	equilibrium
$\vec{e}_r$	flux surface normal vector	equilibrium
$r = r(\vec{x})$	mapping	equilibrium
n, n_1, n_2	quantum numbers	multiplet
$\mathcal{A}_{ij}$	rate coefficients for CRM	atomic data, transport model
$\mathbf{A}$	CRM transition matrix	atomic data, transport model
A_π, $A_{\sigma\pm}$	Einstein coefficients	atomic data
$\vec{x}$	real space coordinate for observation volume	setting (beam line, line of sight)
s	beam coordinate, line-of-sight coordinate	setting (beam line, line of sight)
P_b	beam power	setting (NBI)
E	beam energy	setting (NBI)
$\vec{v}_b$, v_b	beam velocity (E)	setting (NBI)
$\alpha_{E,E/2,E/3}$	beam composition	setting (NBI)
γ_b	beam divergence	setting (NBI)
$\mathcal{M}$	Müller matrix	setting (observation)
$\mathbf{\Pi}$	chain of Müller matrices	setting (observation)
ς	CCD sensitivity	setting (observation)
A_s	spectrometer entrance area	setting (observation)
Ω_m	minimum solid angle of detector	setting (observation)
$\mathcal{T}$	etendue	setting (observation)
ζ	observation angle	setting (observation)
$\mathcal{P}$	line profile	setting, plasma
τ	transmission	setting (observation)

TABLE II: Summary of input model parameters (settings) for the MSE forward model.

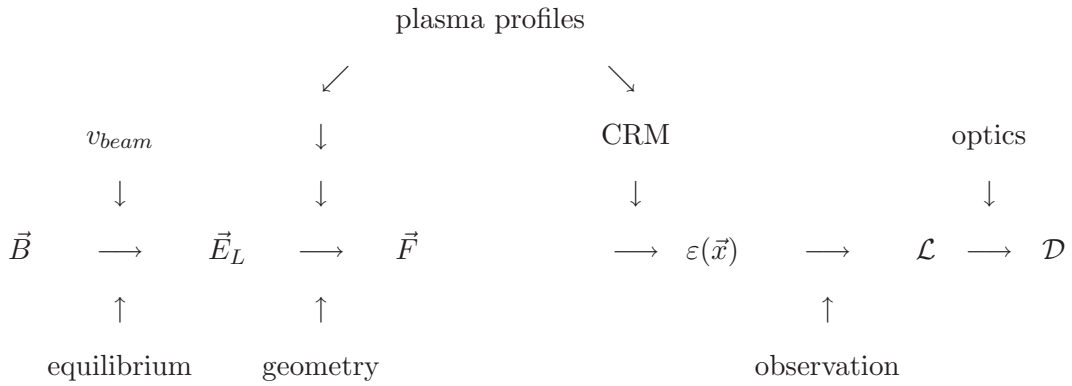

FIG. 1: Schematic flow-chart representing the forward model of spectral MSE measurements. CRM: collisional-radiative model, $\vec{B}$: magnetic field, v_{beam}: beam velocity, $\vec{E}_L$: Lorentz field, $\vec{F}$: total electric field in the moving frame, $\varepsilon(\vec{x})$: local emission coefficient, $\mathcal{L}$: radiance, $\mathcal{D}$: data

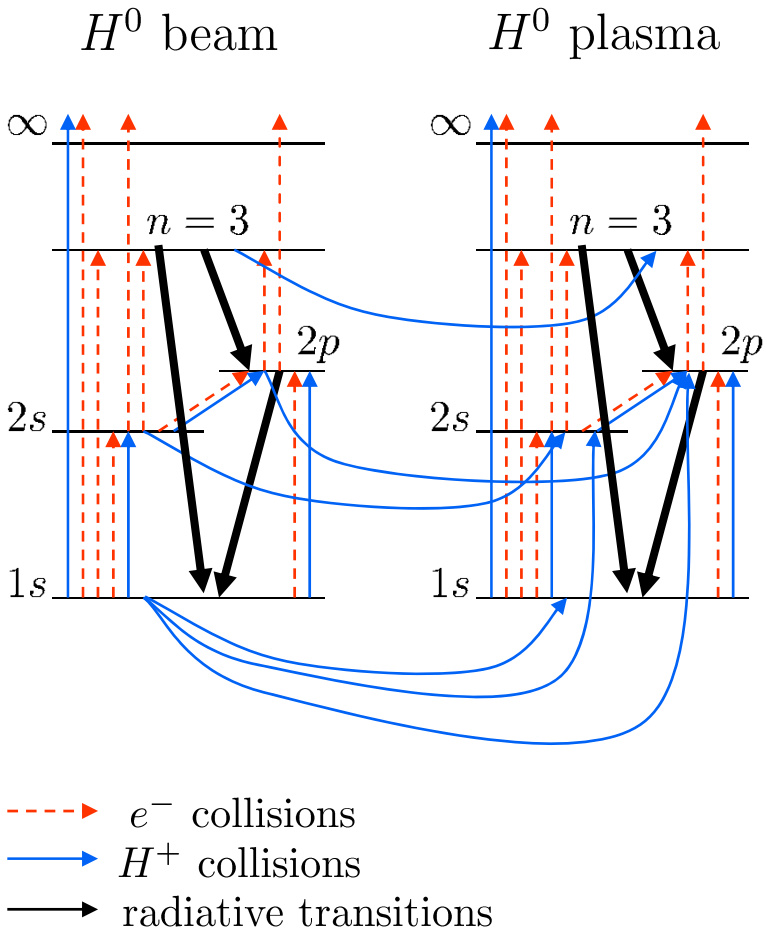

FIG. 2: Simplified Grotian diagram representing the collisional radiative model for the simulation of MSE spectra.

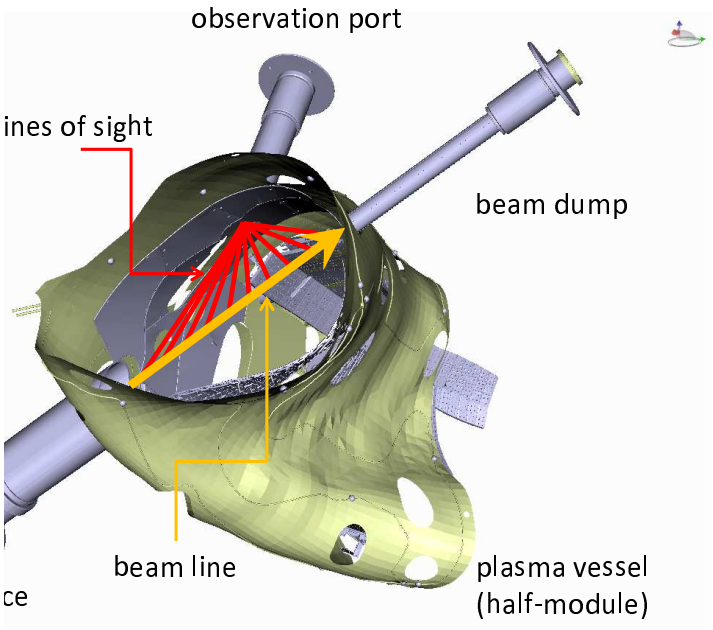

FIG. 3: 3D-CAD view on the diagnostic beam-line and possible observation geometry of a spectral MSE measurement on W7-X (as used for the simulations).

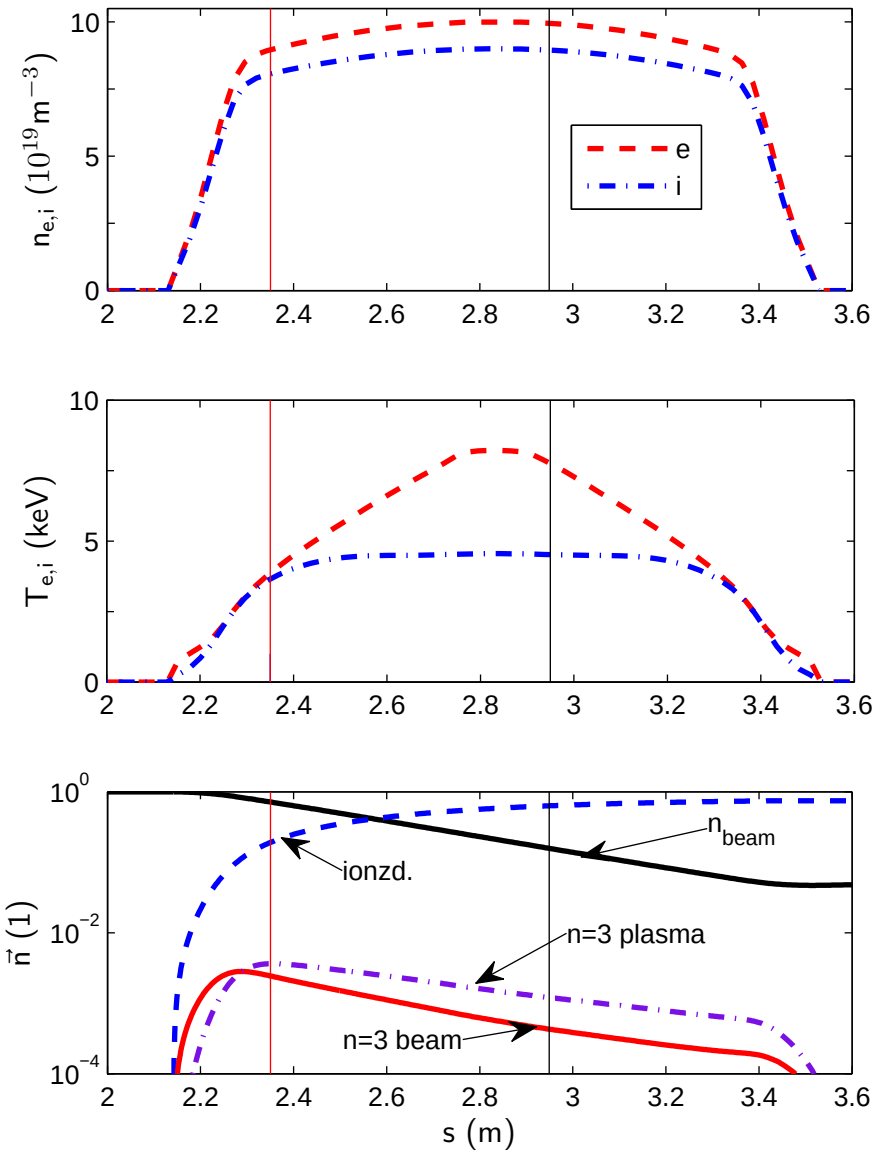

FIG. 4: Upper and mid plot: density and temperature profiles along the beam line of the W7-X diagnostic beam (60 kV H-beam) from predictive transport simulations. The lower plot shows CRM results from fractions for light emitting ($n = 3$) particles from beam (full energy) and plasma and the profile of ionized beam particles and the beam particles. Zero of the beam-line coordinate s is at the position of the ion-source. The vertical lines indicate the position of channels discussed below.

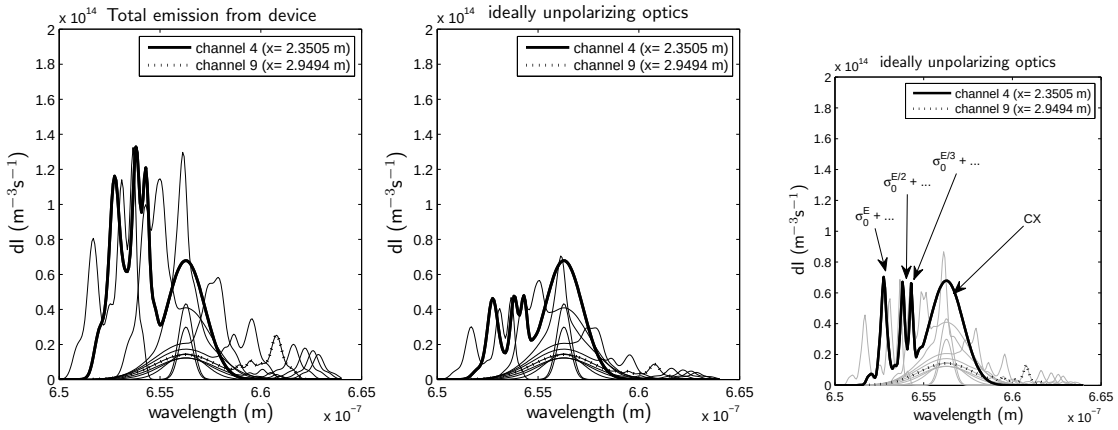

FIG. 5: Simulation of MSE spectra for Wendelstein 7-X (60 keV H^0 diagnostics beam, beam intensity ratios $I_E : I_{E/2} : I_{E/3} = 0.7 : 0.15 : 0.15$, beam divergence 1 degree). The panels show different observation channels; the total shift corresponds to the beam coordinate reflecting the Doppler shift of the spectrum. The left panel shows the total emission from the plasma, the center panel encounters for emission anisotropy and rotation. The right panel corresponds to the central plot but at half of the beam divergence.The labels in the right plot indicate representatively the peaks mainly from σ-lines of full, half and third energy beam emission. The unpolarized charge exchange component is indicated by CX. The peak positions apply for this figure and Fig. 6.

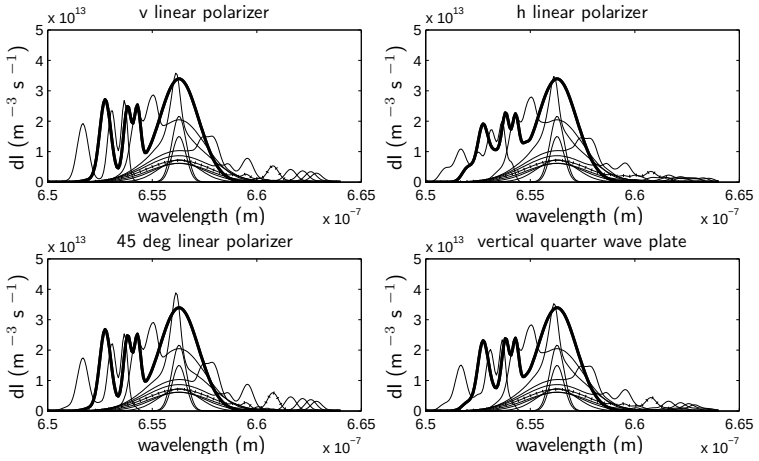

FIG. 6: Simulation of MSE spectra observation (corresponds to central panel in Fig. 5). v and h are vertical and horizontal polarizers, respectively.

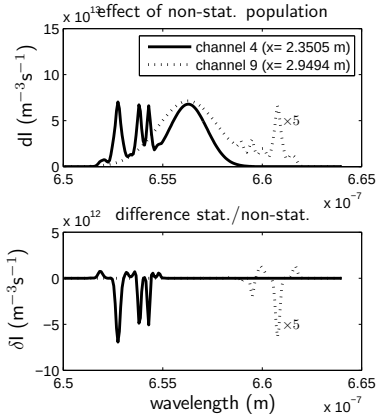

FIG. 7: Simulation of MSE spectra with non-statistical multiplets (to be compared with Fig. 5 right panel). The lower panel shows the difference of spectra from statistical (Fig.5, right panel) to non-statistical distribution (upper panel).

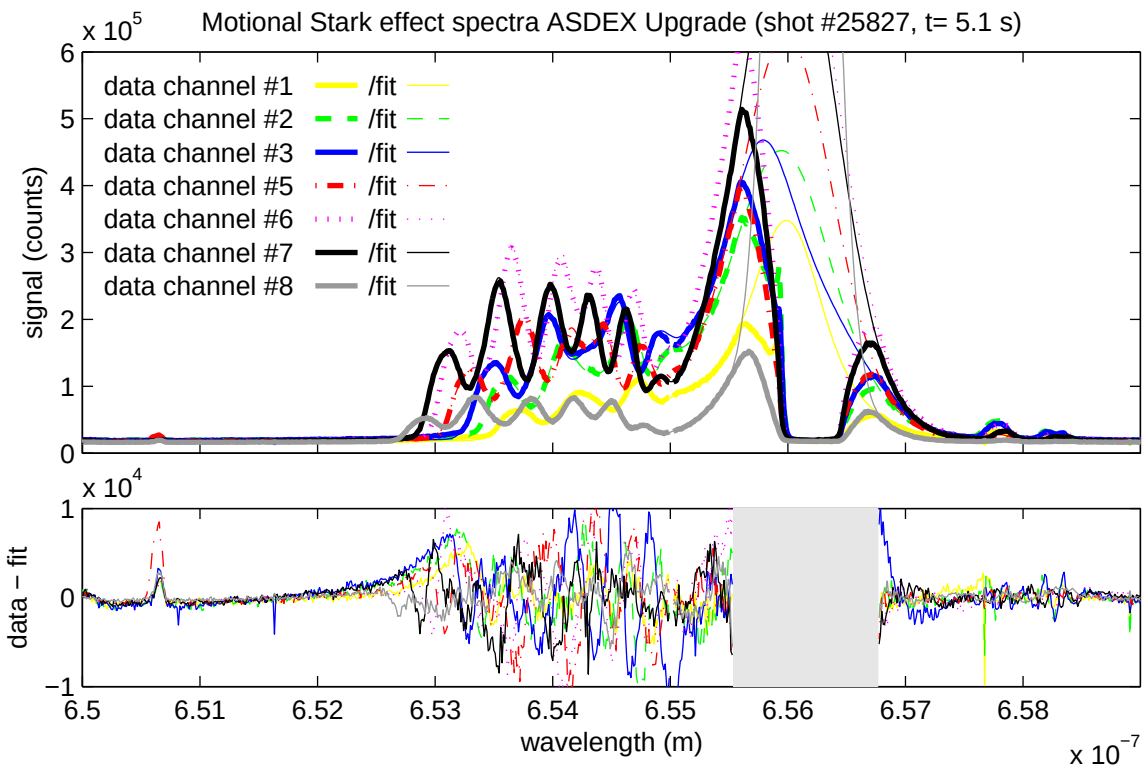

FIG. 8: Experimental MSE spectra and fits of the forward model to the data. The lower panel shows the residuum.